Dynamics of Electrostatic Inchworm Motors for Silicon Microrobots

Daniel S. Contreras, Kristofer S. J. Pister
Berkeley Sensor and Actuator Center
University of California, Berkeley
Berkeley, California, 94720
Email: dscontreras@berkeley.edu

Abstract—We present work on characterizing the speed of electrostatic actuators for applications in microelectromechanical systems (MEMS) based microrobotics. The actuators are based on electrostatic gap closers working in an inchworm motor configuration and fabricated in silicon. Measurements are taken using sidewall contacts on the gap stops of our devices. We have shown that our electrostatic gap closers can operate over a full cycle within 57μs, corresponding to an operational frequency of 17.5kHz. Using similar electrical sidewall contact measurements in the motors, we can measure the speed of the motor shuttles. By operating the gap closing actuators at 8kHz the inchworm motor shuttle can approach speeds over 30mm/s, over 6 times what has been previously reported using optical measurements.

I. Introduction

Millimeter scale robotics has seen great strides in the last two decades in terms of flying [1], [2] and ground based robots [3]–[7]. The current state of the art for autonomous walking microrobots is limited by a lack of low-power, high force, large displacement actuators.

Electrostatic inchworm motors offer power benefits to the world of small-scale robotics. With no static current draw and scale invariant force output, these motors are an attractive solution to microscale actuation. A previous silicon electrostatic inchworm motor based robot showed promise in terms of integrating actuators, mobility mechanisms, and onboard power but was ultimately not able to walk [8]. Using a similar high-voltage CMOS and solar cell process found in [9], we will build on this platform with improved motors and legs.

Previous work demonstrated planar silicon pin-joints [10], [11]. Using these joints, we demonstrated a single-legged robot capable of taking steps under external power using linkages actuated by inchworm motors [12]. By combining electrostatic inchworm motors with these silicon pin-joints we aim to build a multichip robot, depicted in Fig. 1. In order to understand the design trade offs between force and power output we require a well formed theory on the speed limitations of these motors.

Although the speed of GCA's for microrobots has yet to be thoroughly investigated, work has been done to model the dynamics of MEMS relay switches [13]. Using similar models, we build a theory for the speed of our actuators. Using this model we can look deeper into optimizing inchworm motors focusing on an ideal combination of force and power depending on the task the motor will perform.
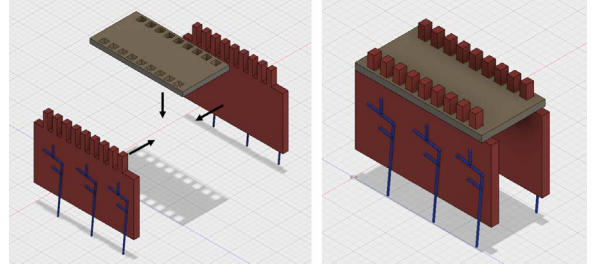

Fig. 1. A multichip robot design. Two chips with three actuated legs each are oriented standing up and a third chip is brought down to add support and routing to the legs. The leg and top routing chips are all fabricated in a single mask silicon process
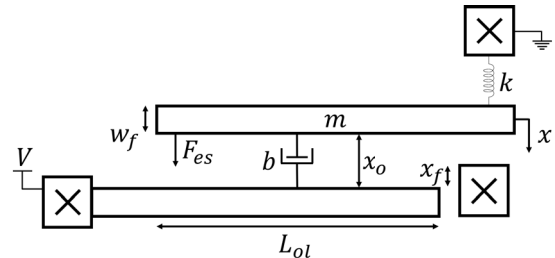

Fig. 2. The free body diagram of an electrostatic gap closing actuator. It is actuated at a voltage V. L_{ol} is the length that the fingers overlap each other. w_f is the finger width and T is the finger thickness into the page

II. Theory

A. Gap Closer Dynamics

The free body diagram of the single cell of a GCA is shown in Fig. 2. The forcing equation for a GCA is given by

$$m\ddot{x} + b\dot{x} + kx = F_{es} \qquad (1)$$

where x is the displacement of the finger, m is the mass of the moving portion of the GCA, b is the damping coefficient, k is the spring constant of the support spring, and F_{es} is the electrostatic actuation force. x_o is the initial size of the gap, before actuation. A gapstop is positioned to maintain a final finger separation of x_f.

In terms of damping, considering the aspect ratio of our structures of 20:1 and gap sizes approaching 1μm, we assume that squeeze film between the actuator fingers will dominate.

The damping coefficient between approximately rectangular plates can be approximated by [14]

$$b = \frac{\mu S_1 S_2^3 \beta(\eta)}{(x_o - x)^3} \quad (2)$$

where μ is the viscosity of air (1.85×10^{-5}Ns/m for our approximations), S_1 is the longer dimension of the plate, S_2 is the shorter dimension of the plate, $\eta = \frac{S_2}{S_1}$ is the aspect ratio of the finger, and $\beta(\eta)$ is a correction factor that depends on η. Depending on the dimensions of the fingers, $S_1 = \max(L_{ol}, T)$ and $S_2 = \min(L_{ol}, T)$. The denominator, $(x_o - x)^3$, is the size of the gap. A GCA contains N number of gaps, which should be factored into the forcing function.

The movable fingers are supported by two parallel fixed guided beams. The spring constant is determined from simple beam theory to be

$$k = \frac{2ETw_s^3}{L_s^3} \quad (3)$$

where E is the Young's Modulus of silicon (169N/m^2 for our approximations), T is the thickness of the device layer, w_s is the width of the beam, and L_s is the length of the beam.

The electrostatic force is found from the changing capacitance between the plates and is given by

$$F_{es} = \frac{1}{2}\epsilon_0 L_{ol}TV^2 \left(\frac{1}{(x_o - x)^2} - \frac{1}{(x_b + x)^2} \right) \quad (4)$$

where V is the drive voltage, ϵ_0 is the vacuum permittivity, and x_b is the gap to the adjacent pair of fingers in the array.

We can find the time for the gap to close by solving this differential equation with the initial conditions of $x(t_{pull-in} = 0) = 0$ and $\dot{x}(t_{pull-in} = 0) = 0$. We also have to factor that the gap does not close completely, since there is a gapstop in our structures that keeps the gap from moving below x_f.

The time for the gap to release will be determined by a different forcing equation. For this case, the spring will restore the structure to its nominal position and will be acting counter to the damping and the inertial terms. We get

$$m\ddot{x} + b\dot{x} + kx = 0 \quad (5)$$

We can solve this differential equation with initial conditions of $x(t_{release} = 0) = x_o - x_f$ and $\dot{x}(t_{release} = 0) = 0$ and using the same coefficients as above.

B. Numerical Solution

Numerical solutions were found using MATLAB. The second order differential equation was decomposed into a system of coupled first order differential equations. Feeding this system into the ode45 function we solved for the position over time of the movable gap closer fingers and the time that the fingers hit the gap stop.

Fig. 3 shows the plots of the position of the GCA over time for both pull-in and release for the range of finger overlap lengths we used in our experiments. The plots are with respect to the size of the gap. The initial gapsize is about 5.8μm and the gapstop limits the gap to 1μm. From these numerical solutions we have a sense of the time ranges we will see in our experiments.
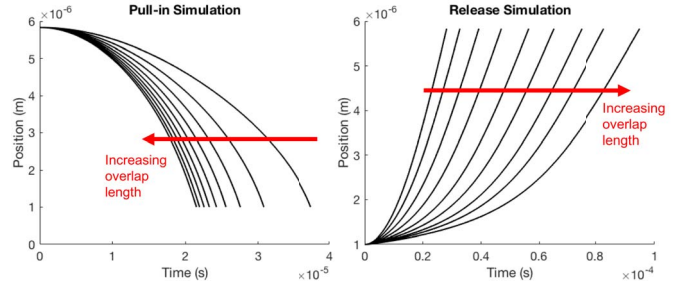

Fig. 3. Plots of the MATLAB solution for pull-in (left) and release (right) positions over time for a GCA. Different lines indicate the varying overlap lengths used in our experiments, red arrows indicate increasing overlap length. In the pull-in plot, the lengths range from the nominal size of $L_{ol} = 76.5$μm to $0.2L_{ol}$ from left to right. In the release plot, the lengths range from $0.2L_{ol}$ to the nominal size of $L_{ol} = 76.5$μm from left to right The pull-in plots shown were taken for $V = 50$V
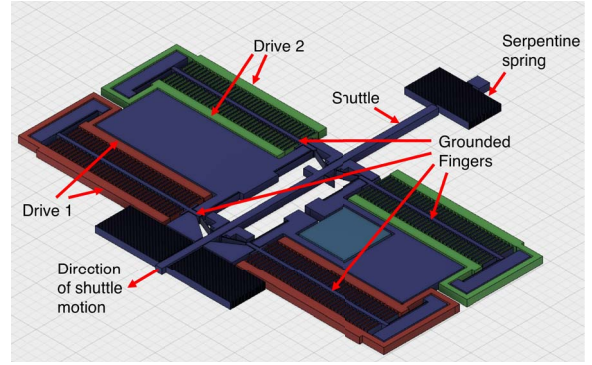

Fig. 4. A model of an inchworm motor. Same signal structures are color-coded. The angled arms attached to the GCAs push the shuttle out in the direction of motion indicated

III. DESIGN AND FABRICATION

A. Inchworm Motor Design

Inchworm motors were designed using the optimization method described in [15]. A 3D model of an inchworm motor is shown in Fig. 4. The motors are composed of 4 GCAs acting in pairs. The GCAs have angled arms attached. When two opposing GCAs close in, the angled arms are able to move the shuttle in one direction. A fabricated inchworm motor is shown in Fig. 5.

These inchworm motors are designed to generate 1mN of force at 80V with a throw of 500μm. Long serpentine springs are used to achieve this throw. Since these motors are unidirectional, these springs also function to reset the motor shuttle's position once the GCAs disengage. They are each designed with a spring constant of 0.1N/m. This assumes that the springs only undergo simple linear motion. A single inchworm shuttle has three serpentine springs attached in parallel for a total stiffness of 0.3N/m. At 500μm of deflection, the springs generate 150μN of force to reset the motor shuttle.

The motors are designed with endstop detection. The shuttle has a cantilever off of its side that will hit another cantilever connected to the endstop detection node once the shuttle
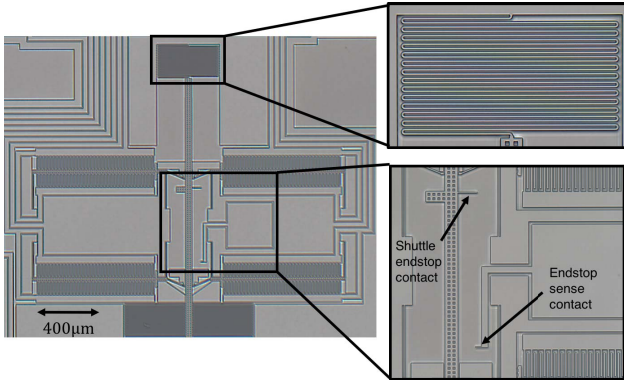
Fig. 5. A photo of a fabricated inchworm motor. A view of the serpentine support spring for the shuttle is shown in the top left. Bottom right shows a detail of the endstop detection structures

travels its full range. A simple cantilever is used so that impact between the structures does not rapidly degrade the contact.

B. GCA Design

A layout view of the GCA alongside a picture of the fabricated device is shown in Fig. 6. This structure is the unit cell of the inchworm motor. An array of moving fingers are attached to a main shuttle that is anchored to the substrate by flexible springs. The drive fingers are attached to the substrate by large anchors which are routed around the structure to the high voltage drive pad. The sense nodes are blocks of silicon adjacent to the moving fingers. The release node has a movable block to perform the release time measurements.
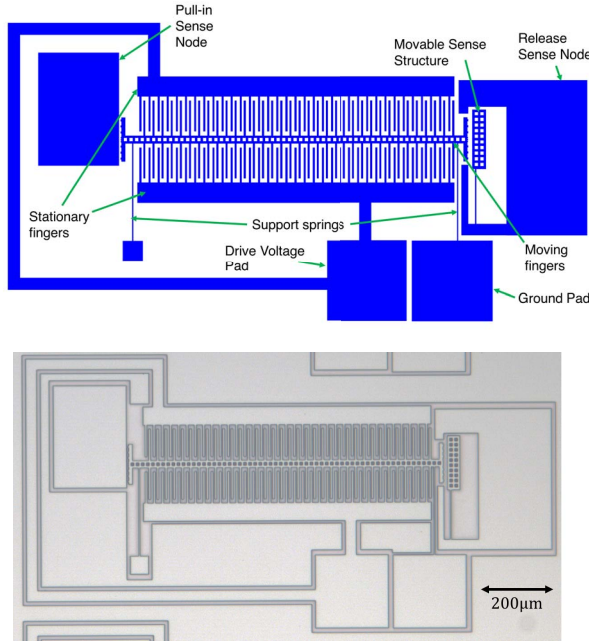

Fig. 6. A layout view of the GCA used for timing measurements (top) and a picture of the actual device (bottom). The sense nodes are tied to 4V through a pull-up resistor

C. Fabrication

Devices are fabricated in a silicon-on-insulator (SOI) process. These SOI wafers have a 40µm device layer, 2µm buried oxide, and 550µm substrate. The structures are etched into the frontside device silicon. Structures are released using a vapor-phase anhydrous hydrogen fluoride etch. Once the structures are fabricated and released, a layer of Au/Pd is sputtered onto the structures. The Au/Pd sputter gives the structures more conductive sidewalls to easily detect signals when the gap closers actuate. The thickness of the final metal layer was approximately 40nm. The sheet resistance was about $10\Omega/\square$.

IV. EXPERIMENTAL METHODS

A. Gap Closer Relay

Finger overlap length and spring stiffness were independently varied in these experiment. Table I shows the various geometries of our structures. The overlap length were varied from 20% the nominal value of 76.5µm up to the full nominal value in increments of 10%. The spring widths were varied in increments of 0.5µm from 1µm to 4.5µm, with 2µm being the nominal value.

Gap closer speed was measured using sidewall contact relays. The gap stop is pulled up to 4V by a resistor. When the GCA is energized, the grounded fingers will move into the gapstop, make contact with the pull-in sense node, and pull that node to ground. The time between the rise in actuation voltage and the change in the sense node is measured on an oscilloscope. Time is measured from the point the actuation signal reaches the previously measured pull-in voltage of the structure to the time the sense signal begins to decay.

To measure the time for the GCA to release a structure must be manually moved to make contact with the movable fingers at the GCAs unactuated position. The sense node has a free structure on a cantilever that is moved into the grounded fingers with a tungsten probe tip. When the GCA is deenergized the springs pull the fingers back to their nominal position and the GCA hits the node. This node is then brought to ground by the movable fingers.

B. Inchworm Motor Shuttle Speed

To measure the motor's shuttle speed, the endstop detection structure was used. In a similar manner to the gapstop relay, the endstop detection node is brought up to 4V through a resistor and when the grounded shuttle contacts the node the voltage drops. The time difference between when the motor
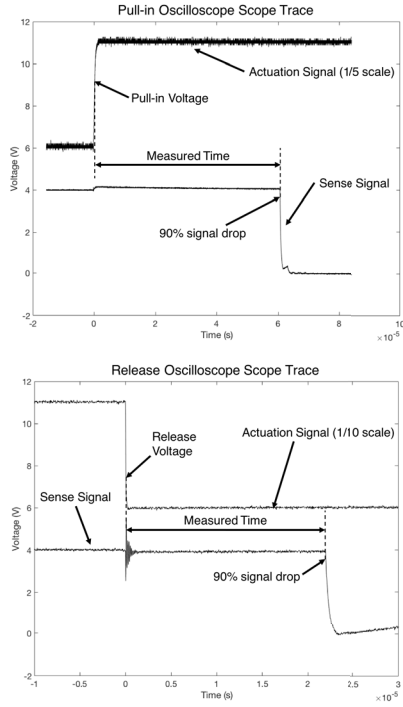
Fig. 7. Oscilloscope trace of the actuation and sense voltage as the GCA pulls-in (top) and releases (bottom). The ringing on the sense signal in the release figure at the time of the actuation voltage drop is caused by capacitive coupling through the probe station used to take these measurements. The pull-in figure was taken on a GCA with the nominal L_{ol} and $k = 7.74$N/m at $V = 25$V (image shows it at $1/5$ scale). The release figure is taken on a GCA with the nominal L_{ol} and $k = 0.97$N/m
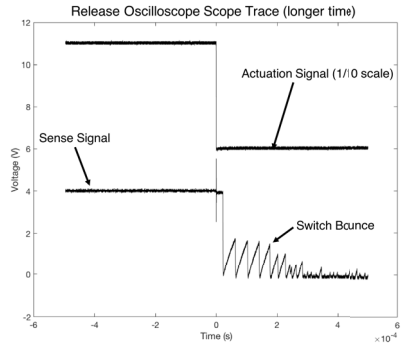

Fig. 8. A larger time scale figure of the release plot shown in 7. Figure shows the bounce of the switch on the sense node when the GCA releases

begins actuating and when the voltage drops is measured on an oscilloscope.

V. EXPERIMENTAL RESULTS

A. Sidewall Relay Contact

Resistances for the pull-in and release contacts were measured using a multimeter. Across the wafer, resistances of 1.3 ± 0.3kΩ were measured.

Examples of the signals used to measure the pull-in and release times are shown in Fig. 7. For each GCA, the pull-in
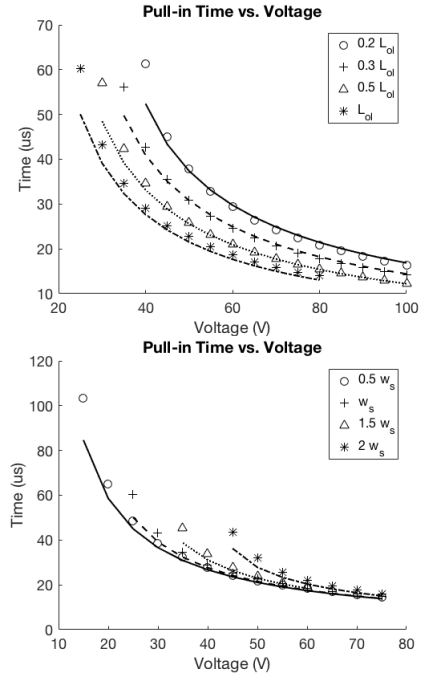

Fig. 9. Pull-in time vs. voltage for gap closer arrays with varying finger overlap length (top) and varying spring stiffness (bottom). Lines indicate numerical results for finger overlap lengths $0.2L_{ol}$, $0.3L_{ol}$, $0.5L_{ol}$ and L_{ol} from top to bottom (top) and spring widths $2w_s$, $1.5w_s$, w_s and $0.5w_s$ from top to bottom (bottom)

voltage and release voltage were measured. The time between when the actuation signal hits these voltages and the sense signal begins to decay is taken as the measured time for the GCA to pull-in and release.

The pull-in sense signal shows a slight rise as the actuation voltage climbs up. This is caused by capacitive coupling through the probe station used to take these measurements. This is the same for the ringing in the release signal as the actuation voltage climbs down. These signal abnormalities exist without the devices in place.

Fig. 8 shows a larger timescale trace of the release signal in Fig. 7. In this signal trace we can see oscillation of the release sense signal as the node drops to zero. This oscillation was apparent on all measurements of release time. This is assumed to be switch bounce caused by the impact of the movable fingers on the release node as the spring resets the fingers to their nominal position.

B. Gap Closer Speed

Fig. 9 shows the dependence of pull-in time on the actuation voltage for varying finger overlap length and varying spring constant. We see good agreement with our dynamic theory and the measured time values.

Fig. 10 shows release time plotted with actuation voltage. The measured release times were faster than what our model predicted, by as much as a factor of three. We can also see a dependence on voltage that was unaccounted for in our model. As the GCA is released at higher voltages the release time
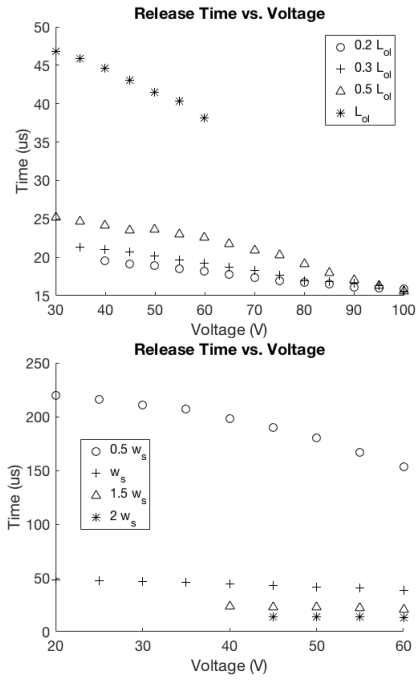
Fig. 10. Release time vs. voltage for gap closer arrays with varying finger overlap length (top) and varying spring stiffness (bottom). We can see that there is a dependence of the release time on the voltage used to actuate the gap closers that was not predicted in our basic mass-damper-spring model. Theoretical values for release time were predicted to be 95μs, 47μs, 33μs, and 28μs for L_{ol}, $0.5L_{ol}$, $0.3L_{ol}$, and $0.2L_{ol}$, respectively and 600μs, 95μs, 36μs, and 20μs for $0.5w_s$, w_s, $1.5w_s$, and $2w_s$ respectively
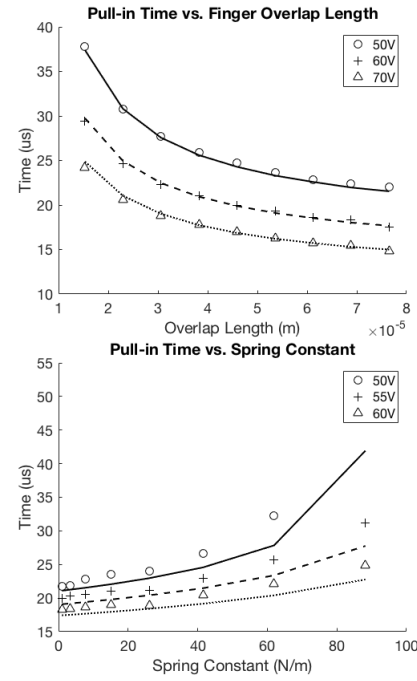

Fig. 11. Pull-in time vs. finger overlap length (top) and spring constant (bottom). Lines indicate numerical results for 50V, 60V, and 70V actuation voltages from top to bottom

gets slightly shorter. It is possible that stress induced in the structure by the electrostatic force could contribute an initial amount of stored energy that leads to a faster releasing time.

We see the dependence of the pull-in time on the finger overlap length and the spring constant in Fig. 11. Again, there is good agreement between the model and the measurements. As the fingers increase in length, the pull-in time is reduced. The pull-in time has a stronger dependence on the electrostatic force than the damping.

Fig. 12 shows the dependence of the release time on the overlap length and spring constant for varying voltages. Despite the model being off in magnitude by large factors the general trend of the release time dependence on the variables seems consistent. Stiffer springs and smaller overlap lengths trend towards shorter release times.

These shorter release times are beneficial. With our nominal structure, the pull-in and release times at 60V are approximately 19μs and 38μs respectively. The frequency for this full operation cycle would be approximately 17.5kHz.

C. Inchworm Motor Shuttle Speed

The measured inchworm motor shuttle speed with respect to GCA frequency is shown in Fig. 13. The inchworm motors tested were designed with the given nominal dimensions of the GCAs. Because we are taking these measurements electrically, we are able to measure much higher speeds than have been previously shown. Operating at 8kHz a shuttle speed

of 35mm/s was measured. This speed is over 6x what has been previously reported for these motors [15]. At and above this frequency the shuttle would not always reach its end of travel. Higher voltages would also lead to breakdown between the fingers.

The relationship between the shuttle speed and the drive frequency was approximately linear. The slope of the linear fit is 4.2μm/s/Hz. This matches expectations since the step size of a single GCA is designed to be 2μm. Within one full inchworm operation cycle both GCAs will engage. This leads to a total 4μm step per cycle.

D. Capacitance Measurements

The gap capacitance was measured using an AD7746 capacitance-to-digital converter. The gap was manually closed using a probe tip. An open capacitance of approximately 0.7pF was measured. The closed gap was measured to be approximately 1.9pF. Running at 100V at 2.5kHz, the motor would consume about 100μW and the shuttle velocity would be 1cm/s.

Parasitic capacitance is also important to consider. For this value, measurements were taken from the drive fingers of a motor to the substrate. This capacitance was approximately 9pF. This capacitance could be greatly reduced by eliminating parts of the substrate beneath the drive fingers. Routing could also be reduced to minimize the substrate capacitance. Currently, signals are routed by long traces and large pads. A better design could reduce these parasitics greatly.
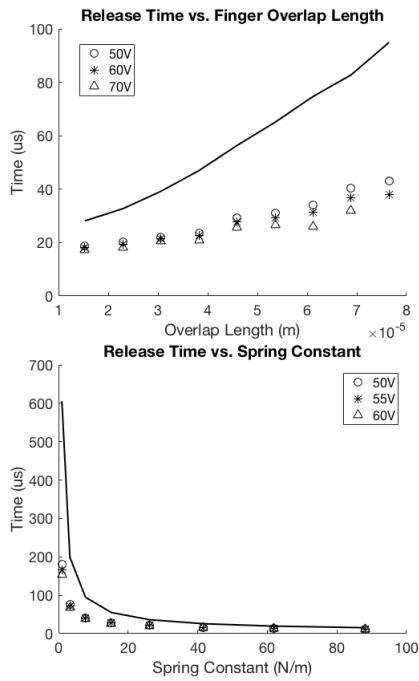
Fig. 12. Release time vs. finger overlap length (top) and spring constant (bottom). The solid lines indicate the numerical result from our model
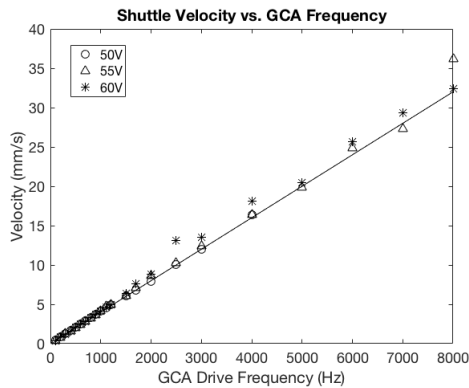

Fig. 13. Inchworm motor shuttle speed vs. the GCA drive frequency

VI. CONCLUSION

Electrostatic MEMS actuators offer a low power solution for autonomous microrobot mobility. Based on our measured data we believe we can safely drive our motors at over 30mm/s with GCAs operating around 8kHz. Taking advantage of mechanical advantage in silicon linkages, we can achieve leg sweep velocities of over 150mm/s for a 5:1 reduction in the force output. If properly designed, the hexapod in Fig. 1 could run at 10s of centimeters per second (10 body lengths/s for a 1cm robot).

Our results have shown good agreement with the pull-in dynamics model and poor agreement with the trend of the release dynamics model. Further characterization of the magnitude discrepancy and voltage dependence of the release dynamics model is necessary. By improving our model we

can optimize motor speed and force output in terms of device geometry. There is still work to be done in optimizing the force density vs. power density of the motors.

REFERENCES

[1] R. J. Wood, "The first takeoff of a biologically inspired at-scale robotic insect," *IEEE transactions on robotics*, vol. 24, no. 2, pp. 341–347, 2008.

[2] D. S. Drew and K. S. J. Pister, "First takeoff of a flying microrobot with no moving parts," in *Manipulation, Automation and Robotics at Small Scales (MARSS) 2017, International Conference on*, Montreal, Canada, 2017.

[3] T. Ebefors, J. U. Mattsson, E. Klvesten, and G. Stemme, "A walking silicon micro-robot," in *Transducers, Solid-State Sensors, Actuators and Microsystems, 10th International Conference on,*, 1999, pp. 1202–1205.

[4] B. R. Donald, C. G. Levey, C. D. McGray, I. Paprotny, and D. Rus, "An untethered, electrostatic, globally controllable MEMS micro-robot," *Journal of microelectromechanical systems*, vol. 15, no. 1, pp. 1–15, 2006.

[5] K. Saito, K. Iwata, Y. Ishihara, K. Sugita, M. Takato, and F. Uchikoba, "Miniaturized Rotary Actuators Using Shape Memory Alloy for Insect-Type MEMS Microrobot," *Micromachines*, vol. 7, no. 4, p. 58, Mar. 2016.

[6] M. Qi, Y. Zhu, Z. Liu, X. Zhang, X. Yan, and L. Lin, "A fast-moving electrostatic crawling insect," in *Micro Electro Mechanical Systems (MEMS), 2017 30th IEEE International Conference on*, Las Vegas, Nevada, USA, Jan. 2017.

[7] D. Vogtmann, R. S. Pierre, and S. Bergbreiter, "A 25 mg magnetically actuated microrobot walking at > 5 body lengths/sec," in *Micro Electro Mechanical Systems (MEMS), 2017 30th IEEE International Conference on*, Las Vegas, Nevada, USA, Jan. 2017.

[8] S. Hollar, A. Flynn, C. Bellew, and K. S. J. Pister, "Solar powered 10 mg silicon robot," in *Micro Electro Mechanical Systems (MEMS), 2003 16th IEEE Int. Conf. on*, Kyoto, Japan, 2003, pp. 706–711.

[9] C. L. Bellew, S. Hollar, and K. S. J. Pister, "An SOI process for fabrication of solar cells, transistors and electrostatic actuators," in *Transducers, Solid-State Sensors, Actuators and Microsystems, 12th International Conference on*, vol. 2, 2003, pp. 1075–1078.

[10] A. M. Mehta and K. S. J. Pister, "Flexure-based two degree-of-freedom legs for walking microrobots," in *ASME 2006 International Mechanical Engineering Congress and Exposition*. American Society of Mechanical Engineers, 2006, pp. 441–450.

[11] D. S. Contreras and K. S. J. Pister, "Durability of silicon pin-joints for microrobotics," in *Manipulation, Automation and Robotics at Small Scales (MARSS) 2016, International Conference on*, Paris, France, 2016.

[12] D. S. Contreras, D. S. Drew, and K. S. J. Pister, "First steps of a millimeter-scale walking silicon robot," in *Transducers, Solid-State Sensors, Actuators and Microsystems, 19th International Conference on*, Kaohsiung, Taiwan, 2017.

[13] P. G. Steeneken, T. G. S. M. Rijks, J. T. M. v. Beek, M. J. E. Ulenaers, J. D. Coster, and R. Puers, "Dynamics and squeeze film gas damping of a capacitive RF MEMS switch," *Journal of Micromechanics and Microengineering*, vol. 15, no. 1, pp. 176–184, Jan. 2005.

[14] M. Bao and H. Yang, "Squeeze film air damping in MEMS," *Sensors and Actuators A: Physical*, vol. 136, pp. 3–27, May 2007.

[15] I. Penskiy and S. Bergbreiter, "Optimized electrostatic inchworm motors using a flexible driving arm," *Journal of Micromechanics and Microengineering*, vol. 23, no. 1, Jan. 2013.